

# A Time-Dependent Random State Approach for Large-scale Density Functional Calculations

Weiqing Zhou<sup>1</sup> and Shengjun Yuan<sup>1,\*</sup>

<sup>1</sup>*Key Laboratory of Artificial Micro- and Nano-structures of Ministry of Education and School of Physics and Technology, Wuhan University, Wuhan 430072, China*

(Dated: January 25, 2023)

We develop a self-consistent first-principle method based on the density functional theory. Physical quantities, such as the density of states, Fermi energy and electron density are obtained using a time-dependent random state method without diagonalization. The numerical error for calculating either global or local variables always scales as  $1/\sqrt{SN_e}$ , where  $N_e$  is the number of electrons and  $S$  is the number of random states, leading to a sublinear computational cost with the system size. In the limit of large systems, one random state could be enough to achieve reasonable accuracy. The method's accuracy and scaling properties are derived analytically and verified numerically in different condensed matter systems. Our time-dependent random state approach provides a powerful strategy for large-scale density functional calculations.

PACS numbers: 31.15.E-; 71.15.-m; 71.15.Mb

Keywords: Density Functional Theory, Random State, Time-dependent Schrödinger Equation, First-principle Calculation

First-principles calculation using the Density Functional Theory (DFT) is one of the most powerful computational methods for multi-electron systems and contributes extensively to physics, chemistry, and material science. DFT theorems prove that there is a one-to-one mapping between the ground-state wave function and the ground-state electron density [1]. In the mid-1960s, Kohn and Sham showed that the finding of the ground-state density could be determined by a set of single-electron equations (Kohn-Sham equations) [2], which is also known as KS-DFT. However, KS-DFT suffers from a size limitation caused by diagonalization, in which the computational cost exhibits a cubic scaling with the system size. Although many efforts, such as iterative diagonalization schemes [3], preconditioned conjugate-gradient minimizations [4–6], and the Car-Parrinello method [7], have improved the scaling behaviour for a relatively small system, it is still hard to handle systems of more than a few hundred or thousand atoms.

This size limitation has stimulated the development of linear-scaling DFT [8–21]. The first attempt can be traced back to the 'divide and conquer' method of Yang [11]. In 1992, Baroni and Giannozzi also proposed an algorithm that determines the electron density directly by using Green's function [12]. In 1993, the density-matrix minimization approach was proposed by Li, Nunes, and Vanderbilt [13]. Following these strategies, many linear-scaling DFT codes have been developed [10, 15–20]. Chebyshev filter method is another successful attempt to reduce the size of the effective dimension of Hilbert space, but there are other non-linear factors dominated in large systems [22]. A linear-scaling algorithm using atomic orbitals (LCAO) basis sets [14] can be applied to suitable systems with clearly separated occupied and empty states [21]. Furthermore, the orbital-free DFT (OF-DFT) [23, 24] is a linear-scaling approach that

avoids complete diagonalization, but the kinetic energy density functionals have not yet reached a good accuracy for many elements [25, 26]. Recently, a linear-scaled DFT is realized by using a stochastic technique in a trace formula [9, 27–30], in which the statistical error of calculating a global variable, such as the total energy (per electron), is reduced by the sample average from different random orbitals. For local quantities, such as the electron density, many stochastic samples are required to reach a reasonable accuracy.

In this letter, we develop a self-consistent first-principle calculation method based on DFT without any diagonalization of the Hamiltonian matrix. The physical quantities, such as the density of states (DOS), Fermi energy and the real-space distribution of electron density, are calculated using the so-called time-dependent random state (TDRS) method. We show that the numerical error of a global or local variable always scales as  $1/\sqrt{SN_e}$ , where  $N_e$  is the number of electrons and  $S$  is the number of random states. It leads to an overall sublinear scaling of the computational costs, and one needs fewer random states for larger systems. The method becomes extremely powerful for massive quantum systems, and a calculation using one random state is enough to achieve reasonable accuracy when  $N_e \rightarrow \infty$ . Our time-dependent random-states DFT (rsDFT) originates from the real-space TDRS method developed in the tight-binding calculations, with an extension from global variables (such as density of states [31], electronic and optical conductivities [32], polarization and screening functions [33], etc.), to a local variable of electron density. It is a general strategy for the local variable calculations and can be applied in the tight-binding model or other physical models as well.

*Density of states and Fermi energy.*— In KS-DFT, the Fermi energy is determined by counting the number of

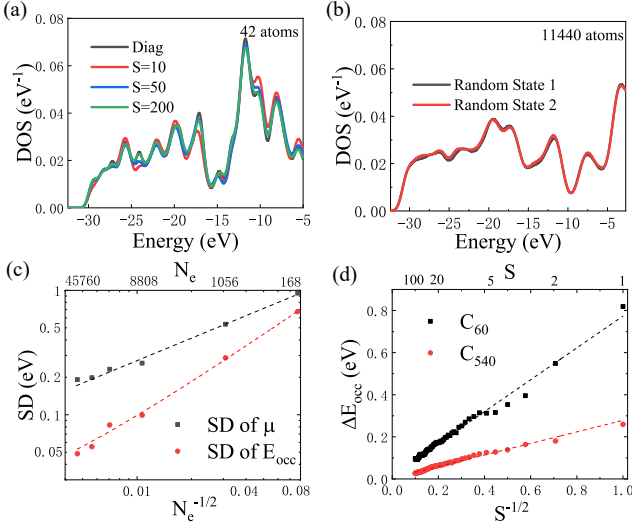


FIG. 1: (a) The DOS of a graphite nanocrystal with 42 atoms, calculated by exact diagonalization or using the TDRS method averaged with a different number ( $S$ ) of random samples. (b) The DOS of a graphite nanocrystal with 11440 atoms was calculated using the TDRS method without random sample averaging. The different colours represent different initial random states. (c) The standard deviations (SD) of  $\mu$  and  $E_{occ}(\mu)$  for graphite nanocrystals with different size ( $N_e$ ), obtained from the statistical analysis of results from 500 individual random states. (d) The error of  $E_{occ}(\mu)$ , with respect to the exact diagonalization, as a function of the number of random states ( $S$ ) used in TDRS for fullerenes  $C_{60}$  and  $C_{540}$ . Here, each point in (d) is averaged from 100 groups of  $S$  random states.

occupied eigenstates, which are obtained from the diagonalization of the Hamiltonian. In rsDFT, the Fermi energy is extracted by the integration of the DOS, which is calculated with the TDRS method without diagonalization [31, 34]:

$$D(\varepsilon) = \frac{1}{2\pi} \int_{-\infty}^{\infty} e^{i\varepsilon t} \langle \varphi | e^{-iHt} | \varphi \rangle dt, \quad (1)$$

here,  $|\varphi\rangle = \sum_i c_i |\mathbf{r}_i\rangle$  is a random state in the real-space and  $\{c_i\}$  are normalized random complex numbers. The state  $|\varphi\rangle$  is also a random superposition state in the energy-space and can be expressed as  $|\varphi\rangle = \sum_n b_n |E_n\rangle$ , where  $b_n = \sum_i c_i a_i^*(E_n)$  and  $a_i(E_n) = \langle \mathbf{r}_i | E_n \rangle$ . Thus Eq. 1, becomes

$$D(\varepsilon) = \sum_{n=1}^N |b_n|^2 \delta(\varepsilon - E_n), \quad (2)$$

where  $N$  is the dimension of the Hamiltonian. For a large but finite  $N$ ,  $|b_n| \rightarrow 1/\sqrt{N}$ , the error of using  $D(\varepsilon)$  to approximate the DOS vanish with  $1/\sqrt{N}$ [31, 34]. As

we normally use the same grid density, the dimension of the Hamiltonian  $N$ , determined by the number of grids, is linearly proportional to the number of atoms and the number of electrons. Thus the numerical error of calculating  $D(\varepsilon)$  scales also with  $1/\sqrt{N_e}$ . The Fermi energy  $\mu$  is determined by  $N_e = \int_{-\infty}^{\mu} D(\varepsilon) d\varepsilon$ . In the case that  $N_e$  is not enough to provide a desired accuracy, additional average of  $D(\varepsilon)$  from different random states ( $|\varphi_p\rangle = \sum_i c_{i,p} |\mathbf{r}_i\rangle$ , where  $p = 1, 2, \dots, S$ ) can be introduced to reduce the statistical error. Then, according to the central limit theory, the overall error of calculating  $D(\varepsilon)$  scales as  $1/\sqrt{SN_e}$ [31, 34]. Numerically, the time-evolution operator  $e^{-iHt}$  can be decomposed using the Chebyshev polynomial method as discussed in Ref. [31, 34], which is unconditionally stable and leads to a linear scaling on the system size as the Hamiltonian  $H$  is a sparse matrix in DFT. The energy resolution is determined by  $1/N_t\tau$ , where  $N_t$  is the number of time steps and  $\tau$  is the time interval ( $dt$ ).

As a numerical check, we calculated the DOS of graphite nanocrystals and fullerene with a different number of carbon atoms. Here, the Kohn-Sham Hamiltonian is constructed with a given initial electron density  $\rho(\mathbf{r})$  as

$$H = -\frac{\nabla^2}{2} + V_{ext}[\rho(\mathbf{r})] + V_H[\rho(\mathbf{r})] + V_{xc}[\rho(\mathbf{r})], \quad (3)$$

where  $-\nabla^2/2$  is the kinetic energy,  $V_{ext}$  is the external potential,  $V_H$  is the Hartree potential, and  $V_{xc}$  is the exchange and correlation potential. The kinetic energy in the KS-Hamiltonian (Eq. (3)) is approximated by using the higher-order finite-difference expansion for the Laplacian operator in a uniform real-space grid [35, 36]. The Hartree potential  $V_H$  is derived by solving the Poisson equation [36]. For exchange and correlation potential  $V_{xc}$ , we use the local density approximation (LDA) [37]. The full ionic potential  $V_{ext}$  is effectively replaced by pseudo-potential in Kleinman-Bylander forms [38].

In Fig. 1(a), we plot the DOS of a graphite nanocrystal with 42 carbon atoms, showing that the TDRS results with more random samples match better to the value from the diagonalization. For large graphite nanocrystals, such as the one with 11440 atoms shown in Fig. 1(b), the TDRS results obtained from two individual random states are quite close to each other. As a quantitative measurement of the statistical error, the standard deviation (SD) of results using only one random state are collected in Fig. 1(c). Here, in each case we considered 500 different random states and plotted the SDs of  $\mu$  and  $E_{occ}(\mu)$  for graphite nanocrystals with different sizes, where  $E_{occ}(\mu)$  is the occupied energy defined as  $E_{occ}(\mu) = \int_{-\infty}^{\mu} \varepsilon D(\varepsilon) d\varepsilon$ . It is clear that the SDs of  $\mu$  and  $E_{occ}(\mu)$  reduce significantly when there are more electrons and approach to zero with an error scales as  $1/\sqrt{N_e}$ . This indicates that for very large systems, it is not necessary to have additional averages with different

random states, and thus using one random initial state is enough to provide a converged result in TDRS. On the other hand, for finite systems such as the fullerenes  $C_{60}$  and  $C_{540}$  shown in Fig. 1(d), the accuracy of using TDRS can be improved by the average using more random states and the result converges to the exact value (from diagonalization) with an error scale as  $1/\sqrt{S}$ . In total, our numerical results prove that the statistical error of using the TDRS method to calculate DOS or related variables scales as  $1/\sqrt{SN_e}$ , just as we expected (see also the error analysis of DOS in the Supplementary Materials).

*Electron density.*— In KS-DFT, the electron density is constructed by the superposition of occupied KS orbitals  $|E_n\rangle$ , namely  $\rho(\mathbf{r}) = \sum_n f(E_n) |E_n(\mathbf{r})|^2$  where  $f$  is the Fermi-Dirac function. In rsDFT, the knowledge of  $|E_n\rangle$  is absent as we do not perform any diagonalization, but  $\rho(\mathbf{r})$  will be obtained in a different way. In the basis of real-space grid,  $\{\mathbf{r}_i\}$ , the wave functions of KS orbitals can be expressed as  $|E_n\rangle = \sum_{i=1}^N a_i(E_n) |\mathbf{r}_i\rangle$ , where  $N$  is the total number of grid points, i.e., the dimension of the Hamiltonian. We consider a random state  $|\varphi\rangle$  in the real space, as the one used in Eq. 1, which is also a random superposition state in the energy space. Thus, a superposition of all occupied states, with a given Fermi energy  $\mu$  and temperature  $T$  can be constructed by applying a Fermi-Dirac (FD) filter on the random state as  $|\varphi\rangle_{FD} \equiv \sqrt{f(H)}|\varphi\rangle = \sum b_n \sqrt{f(E_n)}|E_n\rangle$ , where  $f(H) = 1/(e^{(H-\mu)/k_B T} + 1)$  is the Fermi-Dirac operator. The intensity of state vector  $|\varphi\rangle_{FD}$  at grid  $\mathbf{r}_j$  can be expressed as

$$|\varphi\rangle_{FD}(\mathbf{r}_j)|^2 = \sum_n |b_n|^2 f(E_n) |a_j(E_n)|^2 + \sum_{m \neq n} b_m^* b_n f^{\frac{1}{2}}(E_m) f^{\frac{1}{2}}(E_n) a_j^*(E_m) a_j(E_n). \quad (4)$$

As we see in the calculation of DOS, for a large but finite  $N$ ,  $|b_n| \rightarrow 1/\sqrt{N}$  [39], thus the first term in Eq. 4 converges to  $\rho(\mathbf{r}_j)/N$ , where  $\rho(\mathbf{r}_j) = \sum_n f(E_n) |a_j(E_n)|^2$  is exactly the electron density at grid  $\mathbf{r}_j$ . However, the value of this term is of the order of  $O(N_e/N^2)$ , which is about  $N_e$  times smaller than the second term  $\sim O(N_e^2/N^2)$ . This means that the second term in Eq. 4 becomes dominant when increasing the system size. To approximate  $\rho(\mathbf{r}_j)$  by using  $|\varphi\rangle_{FD}(\mathbf{r}_j)|^2$ , one needs to reduce the second term significantly. This can be realized by using a time-dependent approach in the following way.

Introduce the electron density  $\rho_{RS}(\mathbf{r})$  using a time-dependent RS approach as

$$\rho_{RS}(\mathbf{r}_j) \equiv \frac{N}{2\pi} \int_{-\infty}^{\infty} |e^{-iHt}|\varphi\rangle_{FD}(\mathbf{r}_j)|^2 dt, \quad (5)$$

and one can prove that,  $\rho_{RS}(\mathbf{r})$  converges to  $\rho(\mathbf{r})$  in the limit of  $N \rightarrow \infty$ . Define  $\delta_\rho \equiv \sum_j |\rho_{RS}(\mathbf{r}_j) - \rho(\mathbf{r}_j)|/N_e$  as a measurement error of electron density, and by using the

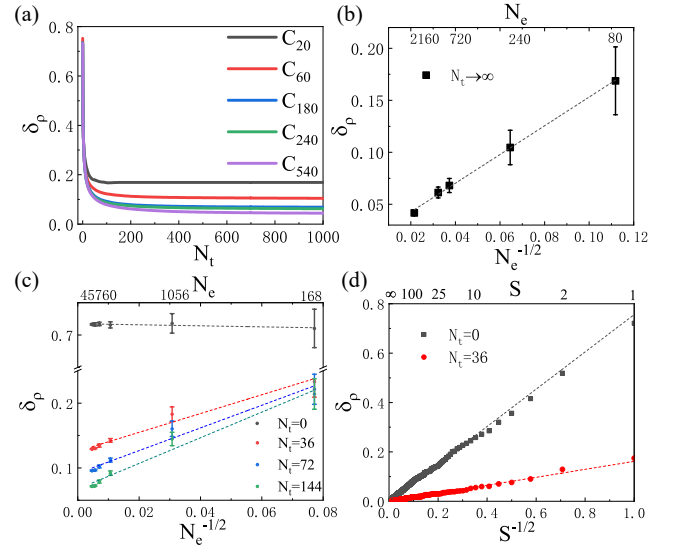


FIG. 2: (a) The statistical error  $\delta_\rho$  as a function of the evolution time  $N_t$  for  $C_{20}$ ,  $C_{60}$ ,  $C_{180}$ ,  $C_{240}$  and  $C_{540}$ , where  $\rho_{Ref}$  is the charge density obtained from diagonalization. The time step is  $\tau = 64\pi$  and the number of random samples  $S = 20$ . (b) The values of  $\delta_\rho$  in (a) in the limit of  $N_t \rightarrow \infty$ , plotted as a function of  $N_e$ . The error bars indicate the corresponding standard deviations. (c) is the same as (b) but with finite  $N_t$ , and the reference charge density is the mean value averaged from 20 random samples with  $N_t = 144$ .  $N_t = 0$  means no time-dependent approach is involved in calculating charge density. (d) The value of  $\delta_\rho$ , plotted as a function of sample number  $S$  for  $C_{60}$ , without or with time-dependent approach ( $\tau = 64\pi$ ).

property  $\int_{-\infty}^{\infty} e^{-i(E_n - E_m)t} dt = 2\pi\delta(E_n - E_m)$ , we have

$$\delta_\rho = \frac{1}{N_e} \sum_j \left| \sum_n (N|b_n|^2 - 1) f(E_n) |a_j(E_n)|^2 + 2\pi N \sum_{m \neq n} b_m^* b_n f^{\frac{1}{2}}(E_m) f^{\frac{1}{2}}(E_n) a_j^*(E_m) a_j(E_n) \delta(E_n - E_m) \right|. \quad (6)$$

For a large but finite  $N$ ,  $|b_n| \rightarrow 1/\sqrt{N}$ , both terms in Eq. 6 converge to zero, but the statistical error of the first and second terms is  $O(1/\sqrt{N})$  and  $O(1/N)$ , respectively. This indicates that in the limit of  $N \rightarrow \infty$ ,  $\rho_{RS}(\mathbf{r})$  converges to  $\rho(\mathbf{r})$ , and  $\delta_\rho$  is dominated by the first term and reduces to zero with a statistical error  $\sim O(1/\sqrt{N})$ .

The accuracy of using Eq. 5 to obtain the electron density can be further improved by averaging  $\rho_{RS}(\mathbf{r})$  from different initial random states. Similar to the calculation of DOS, consider a set of random states  $|\varphi_p\rangle = \sum_i c_{i,p} |\mathbf{r}_i\rangle$ , according to the central limit theorem, for a large but finite  $S$ ,  $\sum_{p=1}^S c_{i,p} c_{i',p}^* / S = E(|c_i|^2) \delta_{i,i'} + O(1/\sqrt{S})$  [34], where  $E(|c_i|^2) \sim 1/N$  is the expectation value of  $|c_i|^2$ . As  $b_n = \sum_{i=1}^N c_i a_i^*(E_n)$ , using the normal-

ization property  $\sum_{i=1}^N |a_i(E_n)|^2 = 1$  and the orthogonal property  $\sum_{i=1}^N a_i(E_n)a_i^*(E_m) = 0$  for  $n \neq m$ , we have  $\sum_p b_{m,p}^* b_{n,p} / S = \delta_{m,n} / N + O(1/\sqrt{S})$ . Thus, together with extra random states average,  $\rho_{RS}(\mathbf{r})$  is an accurate approximation of  $\rho(\mathbf{r})$  with a statistical error  $\delta_\rho$  scales as  $1/\sqrt{SN_e}$ . This scaling behaviour is indeed the same as the calculations of DOS given in Eq. 1.

Here, the time-evolution operator  $e^{-iHt}$  and the Fermi-Dirac filter  $\sqrt{f(H)}$  are carried out numerically using the Chebyshev polynomials[31], which is very efficient and accurate for sparse matrix  $H$  as we discussed in the part of DOS. In the Chebyshev decomposition of the Fermi-Dirac filter, the temperature has to be finite, and we use  $T = 10K$  in all the calculations. The method introduced here becomes more efficient at high temperatures, in which the ground state calculations also involve many states above the Fermi energy due to a nonzero occupation probability given by the Fermi-Dirac distribution. In the following, we show several examples and check the accuracy of obtaining electron density using the TDRS method introduced in Eq. 5.

We first consider fullerene with different numbers of carbon atoms and calculate the charge density for a given Hamiltonian using either the TDRS method or the standard diagonalization. In Fig. 2(a), we plot the statistical error  $\delta_\rho$  as a function of the number of time steps  $N_t$  for  $C_{20}$ ,  $C_{60}$ ,  $C_{180}$ ,  $C_{240}$ , and  $C_{540}$ , where the reference charge density  $\rho$  in each case is the one obtained from the diagonalization. We see that in all cases,  $\delta_\rho$  drops rapidly when introducing the time-evolution, and for a given evolution period (same  $N_t$ ),  $\delta_\rho$  is always smaller in a larger sample. In Fig. 2(b), we plot the minimum value of  $\delta_\rho$  as a function of the number of electrons  $N_e$  in the limit of  $N_t \rightarrow \infty$ . It shows clearly that  $\delta_\rho$  scales exactly as  $O(1/\sqrt{N_e})$ , same as we predicted from Eq. 6. The error bars are the standard deviations of electron density obtained from each individual random initial state, i.e., without any random sample averaging. In practice, it might be numerically expensive to perform a very long evolution, and thus one needs to consider using only finite or relatively small  $N_t$ . Thus we plot in Fig. 2(c) similar results as (b) but with finite  $N_t$ . We see that: (1) in the absence of the time-dependent approach ( $N_t = 0$ ), the value of  $\delta_\rho$  keeps the same amplitude, independent of the system size; (2) when the time-evolution is introduced, the value of  $\delta_\rho$  starts to decrease when increasing the size of the sample ( $N_e$ ). In Fig. 2(d), we consider the influence of sample average on the statistical error by plotting the value of  $\delta_\rho$  as a function of sample number  $S$ . Here the reference charge density is the one obtained from  $C_{60}$  with exact diagonalization, and we see that the scaling of the error follows as  $1/\sqrt{S}$ , for both cases with or without the time-dependent approach. The results presented in Fig. 2 verified numerically that the statistical error of calculating the charge density using the TDRS method

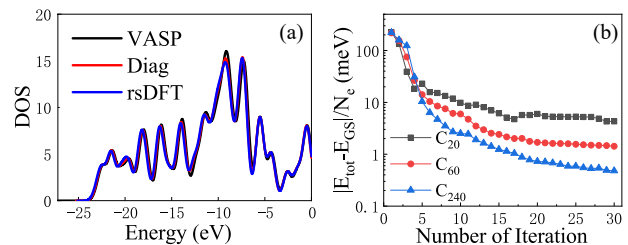


FIG. 3: (a) For  $C_{60}$ , the eigenvalue distribution of the ground state calculated from VASP, diagonalization and rsDFT, respectively. (b) The convergence of the total energy during the iteration for  $C_{20}$ ,  $C_{60}$ , and  $C_{240}$ . Here the total energy of the ground state ( $E_{GS}$ ) is obtained from diagonalization.

scales as  $1/\sqrt{SN_e}$ , with the same scaling behaviour as the calculation of DOS.

*Self-consistent iteration.*— Now, we consider the detailed self-consistent iterations in rsDFT. Here, the numerical results obtained from the widely used commercial KS-DFT package VASP (Vienna Ab initio Simulation Package) [40] are also presented as references.

In Fig. 3(a), we show the ground state DOS of  $C_{60}$  calculated using rsDFT, standard KS-DFT (with diagonalization) and VASP, respectively. Pulay mix is adopted in the iteration to optimize the input density and accelerate the convergence [41]. In rsDFT, we use 10 random samples in DOS calculations and 36 random samples with  $N_t = 36, \tau = 64\pi$  in electron density calculations. The DOS obtained from different approaches agree well, indicating that (1) our DFT code based on diagonalization correctly reproduces the ground state from VASP, (2) the newly proposed rsDFT provides accurate results as these can be obtained from standard KS-DFT and the diagonalization can be completely ruled out in the entire iteration process. In Fig. 3(b), we present more results of converged rsDFT calculations of fullerenes with different sizes, and show the total energy difference compared with the result from diagonalization in each iteration step. In general, the convergence to the ground state is more difficult in the larger system in KS-DFT, requiring more iteration steps to reach the same accuracy for the total energy. In rsDFT, however, the accuracy is increased automatically in larger systems due to the  $1/\sqrt{SN_e}$  dependence of the statistical error, as shown clearly in convergence of the total energy during the iterations in Fig. 3(b).

*Scaling Behavior.*— At last, we check the scaling behaviour of rsDFT. The non-diagonal elements of KS-Hamiltonian are from the kinetic energy and non-local pseudopotentials in Eq. (3), leading to a highly sparse Hamiltonian matrix due to the locality. The number of the non-zero elements in the matrix scales linearly with the number of atoms in the system. In rsDFT, the basic and dominant calculations are the multiplica-

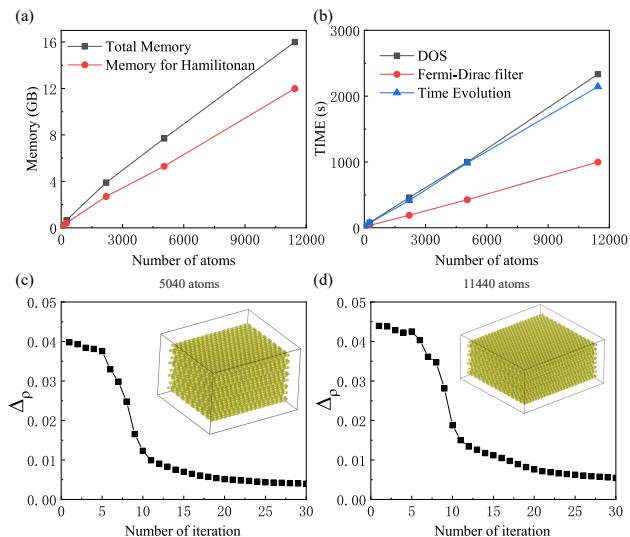


FIG. 4: (a,b) The cost of memory and CPU time in rsDFT for A-B stacked graphite with different numbers of carbon atoms. The black and red curves in (a) are the total memory cost and the memory used to store the sparse Hamiltonian matrix. The black, red and blue curves in (b) correspond to the time cost of one iteration for the calculations of DOS, Fermi-Dirac filter and time-evolution averaging, respectively. (c,d) The difference of input and output electron density as a function of iteration steps for A-B stacked graphite with 5040 and 11,440 atoms, respectively. The insets indicate the converged ground state density.

tions between the Hamiltonian matrix and a state vector, in which the number of operations scales linearly with the nonzero elements in the matrix. Therefore, the total computational load (CPU time) and memory cost of rsDFT are linearly dependent on the dimension of the Hamiltonian, which is proportional to the number of atoms in the system. These linear-scaling behaviours are verified using graphite crystal, with up to 11440 carbon atoms (45760 electrons) in Fig. 4 (a-b). As benchmark tests, we perform complete ground state calculations of graphite with 5040 and 11440 carbon atoms, respectively. The difference of input and output electron density ( $\Delta\rho \equiv \sum_i |\rho_{out}(\mathbf{r}_i) - \rho_{in}(\mathbf{r}_i)|/N$ ) as a function of iterative steps is plotted in Fig. 4 (c-d). In all cases, we used the same calculation parameters, such as the same real-space grid density, and the same accuracy for the Chebyshev decompositions of the time-evolution operator and the Fermi-Dirac filter. One should notice that, for 11440 carbon atoms, the total memory cost is only 16 GB. Due to the linear-scaling behaviour, a self-consistent calculation of millions of atoms should be possible for computer clusters with Terabytes (TB) memory.

*Conclusion and Discussion.*— We developed a sublinear-scaled self-consistent first-principle calculation

method rsDFT. We use a TDRS method to calculate the density of states and determine the Fermi energy. A Fermi-Dirac filter on a random state and, subsequently, a wave propagation according to the time-dependent Schrödinger equation are introduced to approximate the spatial distribution of the electron density. The accuracy can be improved by the average using different initial random states. The overall numerical error of either a global quantity or a local variable scales as  $1/\sqrt{SN_e}$ , where  $N_e$  is the number of electrons and  $S$  is the number of random states. It leads to an overall sublinear scaling of the computational costs, as for larger systems, one needs fewer random states for the sample average. The method becomes extremely powerful when  $N_e \rightarrow \infty$ , and a calculation using one random state is enough to achieve reasonable accuracy.

In the recently developed stochastic DFT (sDFT) [9, 27–30], the physical quantities, such as the Fermi energy and electron density, are calculated using the trace formula of the stochastic technique without diagonalization, i.e., the trace of a variable is approximated by the average of its expectation values in stochastic orbitals. One of the main differences between rsDFT and sDFT is that all the variables in rsDFT are obtained in a more deterministic way based on numerical solutions of the time-dependent Schrödinger equation, which is absent in sDFT. In particular, the dominant noise in the electron density induced by occupied states after the Fermi-Dirac filter is dramatically reduced by the time-dependent approach in rsDFT. A large number of stochastic orbitals (random samples) is required to reduce the statistical error of the electron density in sDFT. And to keep the same accuracy of calculating the local variables such as electron density, one can not use fewer stochastic orbitals for larger systems, even in the limit of  $N_e \rightarrow \infty$ .

In our earlier works, we have developed a so-called tight-binding propagation method (TBPM) for large-scale modelling of complex quantum systems. A direct extension of TBPM in rsDFT is straightforward. For example, by using the TDRS-based method without diagonalization, one can calculate the electronic and optical conductivities [42, 43], polarization and screening functions [32, 44], diffusion coefficient and localization length [33, 44], quasieigenstate [45], and many other applications as implemented in our homemade simulation package, TBPLaS [46]. The main advantage of rsDFT and the other time-dependent methods mentioned above is that there is no diagonalization of the Hamiltonian matrix in the whole process, and the errors of these calculated variables all scale as  $1/\sqrt{SN_e}$ , leading to an overall sublinear scaling on the computational costs. Furthermore, the atomic force can be calculated the same way as the traditional DFT or OF-DFT by using the formulation based on the electron density in real space [47–50]. It is also possible to extract the atomic force using the wave function of approximated ground states, which will

be discussed in future work. The rsDFT provides a new possibility to study large-scale systems from the first-principle calculations and can be used widely in physics, chemistry, biology and material science, with possible extension to large-scale TD-DFT and GW calculations.

*Acknowledgements.*— S.Y. thanks Shiwu Gao, Hans De Raedt, Mikhail Katsnelson, Guodong Yu, and Yalei Zhang for many helpful discussions. This work is supported by the National Nature Science Foundation of China (No. 11974263) and the Supercomputing Center of Wuhan University.

---

\* s.yuan@whu.edu.cn

- [1] P. Hohenberg and W. Kohn, *Inhomogeneous Electron Gas*, *Phys. Rev.* **136**, B864 (1964).
- [2] W. Kohn and L. J. Sham, *Self-Consistent Equations Including Exchange and Correlation Effects*, *Phys. Rev.* **140**, A1133 (1965).
- [3] J. R. Chelikowsky, X. Jing, K. Wu, and Y. Saad, *Molecular dynamics with quantum forces: Vibrational spectra of localized systems*, *Phys. Rev. B* **53**, 12071 (1996).
- [4] A. Edelman and S. T. Smith, *On conjugate gradient-like methods for eigen-like problems*, *BIT Numer. Math* **36**, 494 (1996).
- [5] M. P. Teter, M. C. Payne, and D. C. Allan, *Solution of Schrödinger's equation for large systems*, *Phys. Rev. B* **40**, 12255 (1989).
- [6] M. C. Payne, M. P. Teter, D. C. Allan, T. A. Arias, and J. D. Joannopoulos, *Iterative minimization techniques for ab initio total-energy calculations: molecular dynamics and conjugate gradients*, *Rev. Mod. Phys.* **64**, 1045 (1992).
- [7] R. Car and M. Parrinello, *Unified Approach for Molecular Dynamics and Density-Functional Theory*, *Phys. Rev. Lett.* **55**, 2471 (1985).
- [8] S. Goedecker, *Linear scaling electronic structure methods*, *Rev. Mod. Phys.* **71**, 1085 (1999).
- [9] R. Baer, D. Neuhauser, and E. Rabani, *Self-Averaging Stochastic Kohn-Sham Density-Functional Theory*, *Phys. Rev. Lett.* **111**, 106402 (2013).
- [10] L. O. Jay, H. Kim, Y. Saad, and J. R. Chelikowsky, *Electronic structure calculations for plane-wave codes without diagonalization*, *Comput. Phys. Commun.* **118**, 21 (1999).
- [11] W. Yang, *Direct calculation of electron density in density-functional theory*, *Phys. Rev. Lett.* **66**, 1438 (1991).
- [12] S. Baroni and P. Giannozzi, *Towards very large-scale electronic-structure calculations*, *EPL (Europhysics Letters)* **17**, 547 (1992).
- [13] X.-P. Li, R. W. Nunes, and D. Vanderbilt, *Density-matrix electronic-structure method with linear system-size scaling*, *Phys. Rev. B* **47**, 10891 (1993).
- [14] D. Sánchez-Portal, P. Ordejon, E. Artacho, and J. M. Soler, *Density-functional method for very large systems with LCAO basis sets*, *Int. J. Quantum Chem.* **65**, 453 (1997).
- [15] S. Mohr, L. E. Ratcliff, L. Genovese, D. Caliste, P. Boulanger, S. Goedecker, and T. Deutsch, *Accurate and efficient linear scaling DFT calculations with universal applicability*, *Phys. Chem. Chem. Phys.* **17**, 31360 (2015).
- [16] C. M. Goringe, E. Hernández, M. J. Gillan, and I. J. Bush, *Linear-scaling DFT-pseudopotential calculations on parallel computers*, *Comput. Phys. Commun.* **102**, 1 (1997).
- [17] E. Hernández, M. J. Gillan, and C. M. Goringe, *Linear-scaling density-functional-theory technique: The density-matrix approach*, *Phys. Rev. B* **53**, 7147 (1996).
- [18] N. D. Hine, P. D. Haynes, A. A. Mostofi, C.-K. Skylaris, and M. C. Payne, *Linear-scaling density-functional theory with tens of thousands of atoms: Expanding the scope and scale of calculations with ONETEP*, *Comput. Phys. Commun.* **180**, 1041 (2009).
- [19] J. VandeVondele, M. Krack, F. Mohamed, M. Parrinello, T. Chassaing, and J. Hutter, *Quickstep: Fast and accurate density functional calculations using a mixed Gaussian and plane waves approach*, *Comput. Phys. Commun.* **167**, 103 (2005).
- [20] S. Ghosh and P. Suryanarayana, *SPARC: Accurate and efficient finite-difference formulation and parallel implementation of Density Functional Theory: Extended systems*, *Comput. Phys. Commun.* **216**, 109 (2017).
- [21] J. M. Soler, E. Artacho, J. D. Gale, A. García, J. Junquera, P. Ordejón, and D. Sánchez-Portal, *The SIESTA method for ab initio order-N materials simulation*, *J. Phys. Condens. Matter* **14**, 2745 (2002).
- [22] V. Michaud-Rioux, L. Zhang, and H. Guo, *RESCU: A real space electronic structure method*, *J. Comput. Phys.* **307**, 593 (2016).
- [23] T. A. Wesolowski and Y. A. Wang, *Recent progress in orbital-free density functional theory* (World Scientific, 2013).
- [24] V. L. Lignères and E. A. Carter, *An introduction to orbital-free density functional theory* (Springer, 2005) pp. 137–148.
- [25] B. Zhou, V. L. Lignères, and E. A. Carter, *Improving the orbital-free density functional theory description of covalent materials*, *J. Chem. Phys.* **122**, 044103 (2005).
- [26] Y. A. Wang and E. A. Carter, *Orbital-free kinetic energy density functional theory* (Springer, 2002) pp. 117–184.
- [27] M. Chen, R. Baer, D. Neuhauser, and E. Rabani, *Overlapped embedded fragment stochastic density functional theory for covalently-bonded materials*, *J. Chem. Phys.* **150**, 034106 (2019).
- [28] M. Chen, R. Baer, D. Neuhauser, and E. Rabani, *Energy window stochastic density functional theory*, *J. Chem. Phys.* **151**, 114116 (2019).
- [29] M. Chen, R. Baer, D. Neuhauser, and E. Rabani, *Stochastic density functional theory: Real-and energy-space fragmentation for noise reduction*, *J. Chem. Phys.* **154**, 204108 (2021).
- [30] A. J. White and L. A. Collins, *Phys. Rev. Lett.* **125**, 055002 (2020).
- [31] S. Yuan, H. De Raedt, and M. I. Katsnelson, *Modeling electronic structure and transport properties of graphene with resonant scattering centers*, *Phys. Rev. B* **82**, 115448 (2010).
- [32] S. Yuan, R. Roldán, and M. I. Katsnelson, *Excitation spectrum and high-energy plasmons in single-layer and multilayer graphene*, *Phys. Rev. B* **84**, 035439 (2011).
- [33] R. Logemann, K. J. A. Reijnders, T. Tudorovskiy, M. I. Katsnelson, and S. Yuan, *Modeling Klein tunneling and caustics of electron waves in graphene*, *Phys. Rev. B* **91**,

- 045420 (2015).
- [34] A. Hams and H. De Raedt, *Fast algorithm for finding the eigenvalue distribution of very large matrices*, *Phys. Rev. E* **62**, 4365 (2000).
- [35] J. R. Chelikowsky, N. Troullier, and Y. Saad, *Phys. Rev. Lett.* **72**, 1240 (1994).
- [36] J. R. Chelikowsky, N. Troullier, K. Wu, and Y. Saad, *Higher-order finite-difference pseudopotential method: An application to diatomic molecules*, *Phys. Rev. B* **50**, 11355 (1994).
- [37] S. H. Vosko, L. Wilk, and M. Nusair, *Accurate spin-dependent electron liquid correlation energies for local spin density calculations: a critical analysis*, *Can. J. Phys.* **58**, 1200 (1980).
- [38] L. Kleinman and D. M. Bylander, *Efficacious Form for Model Pseudopotentials*, *Phys. Rev. Lett.* **48**, 1425 (1982).
- [39] F. Jin, D. Willsch, M. Willsch, H. Lagemann, K. Michielsen, and H. De Raedt, *Random state technology*, *J. Phys. Soc. Jpn.* **90**, 012001 (2021).
- [40] G. Kresse and J. Furthmüller, *Efficiency of ab-initio total energy calculations for metals and semiconductors using a plane-wave basis set*, *Comput. Mater. Sci.* **6**, 15 (1996).
- [41] P. Pulay, *Improved SCF convergence acceleration*, *J. Comput. Chem.* **3**, 556 (1982).
- [42] S. Yuan, M. Rösner, A. Schulz, T. O. Wehling, and M. I. Katsnelson, *Electronic Structures and Optical Properties of Partially and Fully Fluorinated Graphene*, *Phys. Rev. Lett.* **114**, 047403 (2015).
- [43] S. Yuan, H. De Raedt, and M. I. Katsnelson, *Electronic transport in disordered bilayer and trilayer graphene*, *Phys. Rev. B* **82**, 235409 (2010).
- [44] S. Yuan, T. O. Wehling, A. I. Lichtenstein, and M. I. Katsnelson, *Phys. Rev. Lett.* **109**, 156601 (2012).
- [45] H. Shi, Z. Zhan, Z. Qi, K. Huang, E. v. Veen, J. Á. Silva-Guillén, R. Zhang, P. Li, K. Xie, H. Ji, *et al.*, *Large-area, periodic, and tunable intrinsic pseudo-magnetic fields in low-angle twisted bilayer graphene*, *Nat. Commun.* **11**, 1 (2020).
- [46] Y. Li, Z. Zhan, X. Kuang, Y. Li, and S. Yuan, *TBPLaS: a Tight-Binding Package for Large-scale Simulation*, *Comput. Phys. Commun.* , 108632 (2023).
- [47] X. Shao, Q. Xu, S. Wang, J. Lv, Y. Wang, and Y. Ma, *Large-scale ab initio simulations for periodic system*, *Comput. Phys. Commun.* **233**, 78 (2018).
- [48] G. S. Ho, V. L. Lignères, and E. A. Carter, *Introducing PROFESS: A new program for orbital-free density functional theory calculations*, *Comput. Phys. Commun.* **179**, 839 (2008).
- [49] P. Golub and S. Manzhos, *CONUNDrum: A program for orbital-free density functional theory calculations*, *Comput. Phys. Commun.* **256**, 107365 (2020).
- [50] E. Arnon, E. Rabani, D. Neuhauser, and R. Baer, *Equilibrium configurations of large nanostructures using the embedded saturated-fragments stochastic density functional theory*, *J. Chem. Phys.* **146**, 224111 (2017).

# Supplementary Materials: A Time-Dependent Random State Approach for Large-scale Density Functional Calculations

Weiying Zhou<sup>1</sup> and Shengjun Yuan<sup>1,\*</sup>

<sup>1</sup>*Key Laboratory of Artificial Micro- and Nano-structures of Ministry of Education and School of Physics and Technology, Wuhan University, Wuhan 430072, China*

## 1. Higher-order Finite-difference Pseudopotential Method

Within the non-relativistic Kohn–Sham DFT, the ground state of a system of  $N_e$  electrons subject to an external potential can be obtained by solving a set of one-particle equations, the Kohn–Sham equations (atomic units will be used throughout):

$$\left[-\frac{\nabla^2}{2} + V_{KS}[\rho(\mathbf{r})]\right]\varphi_i(\mathbf{r}) = \varepsilon_i\varphi_i(\mathbf{r}) \quad (1)$$

where Kohn-Sham potential  $V_{KS}[\rho(\mathbf{r})]$  is usually divided as:

$$V_{KS}[\rho(\mathbf{r})] = V_{ext}[\rho(\mathbf{r})] + V_H[\rho(\mathbf{r})] + V_{xc}[\rho(\mathbf{r})] \quad (2)$$

where  $V_{ext}$  is the external potential,  $V_H$  is the Hartree potential, and  $V_{xc}$  is the exchange and correlation potential. In this paper, we implement real-space finite-element methods, resulting in  $V_{KS}[\rho(\mathbf{r})] = V_{KS}(\mathbf{r})$ .

In our letter, we impose a simple, uniform orthogonal three-dimensional (3D) grid where the points are described in a finite domain by  $(x_i, y_j, z_k)$  [1]. Kinetic-energy operator can be described by high-order finite-element difference method [2],

$$\frac{\partial^2 \varphi}{\partial x^2} = \sum_{n=-N_h}^{N_h} C_n \varphi(x_i + nh, y_j, z_k) + O(h^{2N_h+2}) \quad (3)$$

where  $h$  is the grid spacing and  $N_h$  is the order of finite-element difference. Expansion coefficients  $C_n$  for a uniform grid are given in Table. S1 [2].

TABLE S1: Expansion coefficients  $C_n$  for higher-order finite-difference expressions of the second derivative.

	$C_i$	$C_{i\pm 1}$	$C_{i\pm 2}$	$C_{i\pm 3}$	$C_{i\pm 4}$	$C_{i\pm 5}$	$C_{i\pm 6}$
$N_h = 1$	-2	1					
$N_h = 2$	$-\frac{5}{2}$	$\frac{4}{3}$	$-\frac{1}{12}$				
$N_h = 3$	$-\frac{49}{18}$	$\frac{3}{2}$	$-\frac{3}{20}$	$\frac{1}{90}$			
$N_h = 4$	$-\frac{205}{72}$	$\frac{8}{5}$	$-\frac{1}{5}$	$\frac{8}{315}$	$-\frac{1}{560}$		
$N_h = 5$	$-\frac{5269}{1800}$	$\frac{5}{3}$	$-\frac{5}{21}$	$\frac{5}{126}$	$-\frac{5}{1008}$	$\frac{1}{3150}$	
$N_h = 6$	$-\frac{5369}{1800}$	$\frac{12}{7}$	$-\frac{15}{56}$	$\frac{10}{189}$	$-\frac{1}{112}$	$\frac{2}{1925}$	$-\frac{1}{16632}$

The Hartree energy density and potential are given by:

$$\varepsilon_H(\mathbf{r}) = \frac{1}{2} \int d\mathbf{r}' \frac{n(\mathbf{r}')}{|\mathbf{r} - \mathbf{r}'|} \quad (4)$$

$$V_H(\mathbf{r}) = \int d\mathbf{r}' \frac{n(\mathbf{r}')}{|\mathbf{r} - \mathbf{r}'|} \quad (5)$$

The Hartree potential  $V_H$  could be obtained by solving Poisson's equation.

For the exchange-correlation part, we use local-density approximation (LDA):

$$E_{xc}[n] = \int d\mathbf{r} n(\mathbf{r}) \varepsilon_{xc}(n(\mathbf{r})) \quad (6)$$



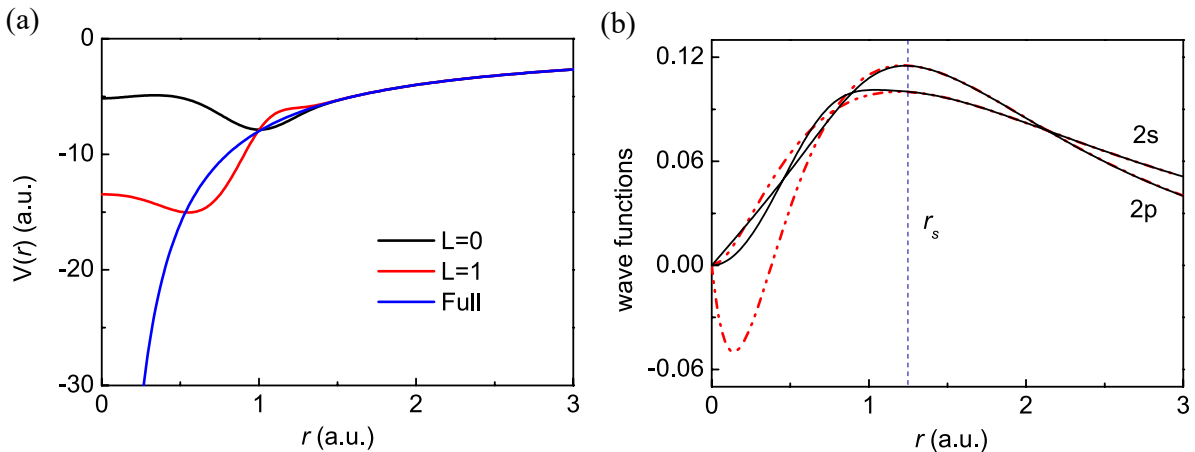


FIG. S1: (a) pseudopotential of carbon atom generated by program ATOM [5]. (b) atomic wavefunction (Red dashed curve) and pseudo-wavefunction (black solid curve) of carbon.

The most accurate formulae for the exchange-correlation functional were obtained by fitting the QMC results for the Jellium model. Various parameterizations are available. We use one of the most popular choices proposed by Vosko-Wilk [3]. From the Jellium model, the local part of the exchange is given by :

$$\begin{aligned} \varepsilon_x &= -\frac{3}{4} \left( \frac{3}{2\pi} \right)^{2/3} \frac{1}{r_s}, \\ V_x &= \left( \frac{3}{2\pi} \right)^{2/3} \frac{1}{r_s}. \end{aligned} \quad (7)$$

For  $V_{ext}(r)$ , we use full ionic potential  $-\frac{Z}{r}$  for the cases of single atoms. For other systems, we implement a pseudopotential operator to reduce the computational demand. We use the projection scheme of the pseudopotential operator suggested by Kleinman and Bylander [4]:

$$V_{ps}(r) = \sum_{a=1}^N \left[ V_{a,ps}^{loc}(r) + \frac{|\Delta V_{a,ps}^l(r) \varphi_{lm}^a\rangle \langle \Delta V_{a,ps}^l(r) \varphi_{lm}^a(r)|}{\langle \varphi_{lm}^a(r) | \Delta V_{a,ps}^l(r) | \varphi_{lm}^a(r) \rangle} \right] \quad (8)$$

where the total pseudopotential can be divided into non-local and local part  $\Delta V_{a,ps}^l(\mathbf{r}) \equiv V_{a,ps}^l(\mathbf{r}) - V_{a,ps}^{loc}(\mathbf{r})$ .  $V_{a,ps}^{loc}$  is the local part with specific angular momentum  $l$  component of atom  $a$ , which differs from zero only in the region smaller than the cutoff radius  $r < r_c$ .  $\varphi_{lm}^a$  is the atomic pseudo wave function with  $lm$  quantum angular momentum numbers. It is worth noticing that the pseudopotential operator only needs to be calculated once at the very beginning since it only depends on the atomic configuration. Taking the carbon atom as an example, we use the program ATOM [5] to generate its pseudopotential. The type of pseudopotential is chosen as local density approximation (LDA) [6] and plotted in Fig. S1. In Fig. S1 (b), we show the atomic pseudo-wave-function, and indeed it is the same as a full-potential wave-function in the range of  $r > r_s$  where  $r_s$  is the cutoff radius. The construction of charge density has been described in the main context.

## 2. Another Fermi-Dirac Filter

In this part, we add some detailed discussion of the methods used in rsDFT. First, we construct a random superposition state in a uniform real-space grid as an initial state,

$$|\varphi_0\rangle = \sum_{i=1}^N c_i |\mathbf{r}_i\rangle, \quad (9)$$

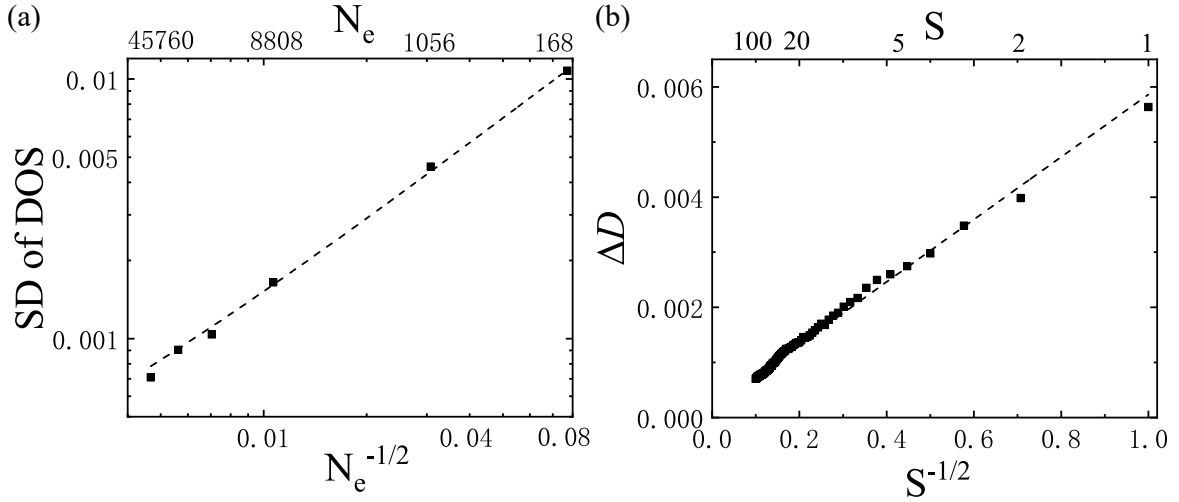


FIG. S2: The statistical error of calculated DOS as a function of the number of electrons for graphite nanocrystals (a) or the number of random states for  $C_{540}$  (b). In (a), the standard deviation of the DOS spectrum  $\int_{-\infty}^{\infty} |D(\varepsilon) - \langle D(\varepsilon) \rangle| d\varepsilon$  is calculated based on the results from 500 individual random states, where  $\langle D(\varepsilon) \rangle$  is the mean value of  $\{D_k(\varepsilon)\}$  with  $k = 1, 2, \dots, 500$ . In (b), the error is defined as  $\Delta D \equiv \int_{-\infty}^{\infty} |D(\varepsilon) - D_{Diag}(\varepsilon)| d\varepsilon$ , where  $D_{Diag}(\varepsilon)$  is the result obtained from the diagonalization, and each point is averaged from 100 groups of  $S$  random states.

where  $N$  is the number of grid,  $\{\mathbf{r}_i\}$  are the real space basis states, and  $\{c_i\}$  are random complex numbers. Assuming that

$$|E_n\rangle = \sum_i^N a_i(E_n)|\mathbf{r}_i\rangle, \quad (10)$$

we have

$$\begin{aligned} |\varphi_0\rangle &= \sum_{i=1}^N c_i \sum_{n=1}^N |E_n\rangle \langle E_n | \mathbf{r}_i \rangle \\ &= \sum_{i=1}^N \sum_{n=1}^N c_i a_i^*(E_n) |E_n\rangle \\ &= \sum_{i=1}^N \sum_{j=1}^N \sum_{n=1}^N c_i a_i^*(E_n) |\mathbf{r}_j\rangle \langle \mathbf{r}_j | E_n \rangle \\ &= \sum_{i=1}^N \sum_{j=1}^N \sum_{n=1}^N c_i a_i^*(E_n) a_j(E_n) |\mathbf{r}_j\rangle. \end{aligned} \quad (11)$$

Now we consider another type of Dirac-Fermi filter different from the one introduced in the main text:

$$\begin{aligned} |\varphi\rangle_{fd} &\equiv f(H)|\varphi_0\rangle \\ &= \sum_{i=1}^N \sum_{j=1}^N \sum_{n=1}^N c_i a_i^*(E_n) f(E_n) a_j(E_n) |\mathbf{r}_j\rangle \end{aligned} \quad (12)$$

In the inner product of  $\langle \varphi_0 | \varphi \rangle_{fd}$  at grid  $\mathbf{r}_j$  can be calculated by using Eq. (11) and Eq. (12),

$$\begin{aligned}
\rho_{fd}(\mathbf{r}_j) &= {}_0 \langle \varphi | \mathbf{r}_j \rangle \langle \mathbf{r}_j | \varphi \rangle_{fd} \\
&= \sum_{i,i'=1}^N \sum_{n,m=1}^N c_i^* a_i(E_n) a_j^*(E_n) c_{i'} a_{i'}^*(E_m) f(E_m) a_j(E_m) \\
&= \sum_{i,i'=1}^N \sum_{n=m}^N c_i^* a_i(E_n) c_{i'} a_{i'}^*(E_n) f(E_n) |a_j(E_n)|^2 \\
&+ \sum_{i,i'=1}^N \sum_{n \neq m}^N c_i^* a_i(E_n) a_j^*(E_n) c_{i'} a_{i'}^*(E_m) f(E_m) a_j(E_m)
\end{aligned} \tag{13}$$

According to the central limit theorem, for a large but finite number ( $S$ ) of the random states  $|\varphi_p\rangle = \sum_i c_{i,p} |\mathbf{r}_i\rangle$ , we have

$$\frac{1}{S} \sum_{p=1}^S c_{i,p} c_{i',p} = E(c^2) \delta_{i,i'} + O\left(\frac{1}{\sqrt{S}}\right). \tag{14}$$

Therefore, one proves that

$$\begin{aligned}
&\lim_{S \rightarrow \infty} \frac{1}{S} \sum_{p=1}^S \langle \varphi_p | \mathbf{r}_j \rangle \langle \mathbf{r}_j | \varphi_p \rangle_{fd} \\
&= \sum_{i=1}^N \sum_{n=1}^N E(|c|^2) f(E_n) |a_i(E_n)|^2 |a_j(E_n)|^2 \\
&+ \sum_{i=1}^N \sum_{n \neq m}^N E(|c|^2) f(E_m) a_i(E_n) a_i^*(E_m) a_j^*(E_n) a_j(E_m) \\
&= \sum_{i=1}^N |a_i(E_n)|^2 \sum_{n=1}^N E(|c|^2) f(E_n) |a_j(E_n)|^2 \\
&= \frac{1}{N} \sum_{n=1}^N f(E_n) |a_j(E_n)|^2 \\
&= \frac{1}{N} \rho_{diag}(\mathbf{x}_j)
\end{aligned} \tag{15}$$

here we used the normalization property of KS orbitals

$$\sum_{i=1}^N |a_i(E_n)|^2 = 1 \tag{16}$$

and the orthogonal property

$$\sum_{i=1}^N a_i(E_n) a_i^*(E_m) = 0 \tag{17}$$

for  $m \neq n$ . Eq. (15) indicates that

$$\rho_{fd}(\mathbf{r}_j) \equiv \frac{N}{S} \sum_{p=1}^S \langle \varphi_p | \mathbf{r}_j \rangle \langle \mathbf{r}_j | \varphi_p \rangle_{fd} \tag{18}$$

is an approximation of the charge density at  $\mathbf{r}_j$  with an error vanishes as  $1/\sqrt{S}$ , which can be verified in the zoom-in figure of Fig. S3 .

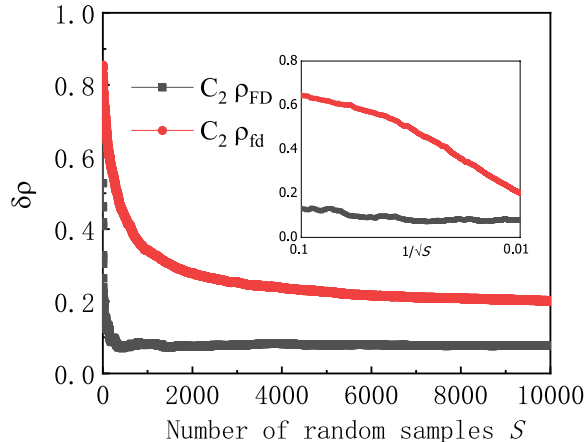


FIG. S3: The difference between the electron density obtained from KS-DFT  $\rho_{diag}$  and rsDFT as a function of the number of random samples  $S$ . In rsDFT, the results are obtained by using  $\rho_{FD}$  (Eq. (4) in the main context) or  $\rho_{fd}$  (Eq. (13)). Using  $\sqrt{f(H)}$  instead of  $f(H)$  in the Fermi-Dirac filter will significantly reduce the statistical error.

However, the converge of  $\rho_{fd}(\mathbf{r}_j)$  using the Fermi-Dirac filter  $f(H)$  is slower than the one using double  $\sqrt{f(H)}$  introduced in the main text. The reason is that, in Eq. (13), the sum in the second term ( $n \neq m$ ) involves all unoccupied states associated with the index  $n$ , and their number is several orders larger than the number of occupied states because  $N \gg N_e$ . To overcome this difficulty, we introduce  $|\varphi\rangle_{FD} = \sqrt{f(H)}|\varphi\rangle_0$ , the one used in the main context. The main advantage of using  $\rho_{FD}(\mathbf{r}_j)$  is that the sums in the second term ( $n \neq m$ ) of Eq. (4) of the main context includes only occupied states, leading to a much faster convergence compared with Eq. (13) (see Fig. S3).

### 3. Chebyshev Polynomials Method

In the numerical calculation, the operators  $\frac{1}{\sqrt{e^{\beta(H-\mu)}+1}}$  and  $e^{-iHt}$  are approximated by using the Chebyshev polynomial method. In general, a function  $f(x)$  whose values are in the range  $[-1,1]$  can be expressed as,

$$f(x) = \frac{1}{2}c_0T_0(x) + \sum_{k=1}^{\infty} c_kT_k(x) \quad (19)$$

where  $T_k(x) = \cos(k \arccos x)$  and the coefficients  $c_k$  are

$$c_k = \frac{2}{\pi} \int_{-1}^1 \frac{dx}{\sqrt{1-x^2}} f(x)T_k(x) \quad (20)$$

if we let  $x = \cos\theta$ , then  $T_k(x) = T_k(\cos\theta) = \cos k\theta$ , and

$$\begin{aligned} c_k &= \frac{2}{\pi} \int_0^\pi f(\cos\theta) \cos k\theta d\theta \\ &= \text{Re} \left[ \frac{2}{N} \sum_{n=0}^{N-1} f\left(\cos \frac{2\pi n}{N}\right) e^{2\pi ink/N} \right], \end{aligned} \quad (21)$$

which can be calculated by the fast Fourier transform (FFT). We normalize  $H$  such that  $\tilde{H} = H/\|H\|$  has eigenvalues in the range  $[-1,1]$  and put  $\tilde{\beta} = \beta/\|\beta\|$ . Then

$$f(\tilde{H}) = \sum_{k=0}^{\infty} c_k T_k(\tilde{H}) \quad (22)$$

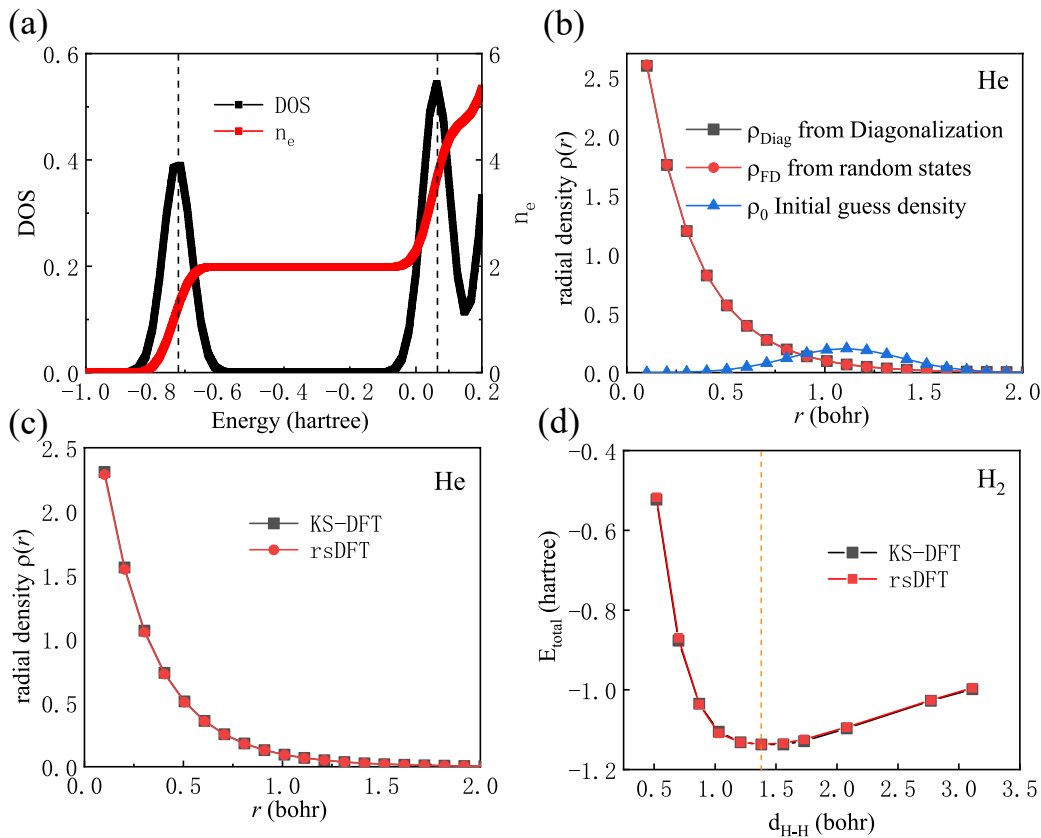


FIG. S4: (a) DOS and carrier density of one He atom calculated using the time-dependent random state method of one He atom. The vertical dashed lines indicate the energies obtained from the diagonalization. (b) The output electron density after one iteration using diagonalization (black) and Fermi-Dirac filter on random states (red) from the same input electron density (blue). For the He atom, due to the spherical symmetry, the electron density is only a function of distance ( $r$ ) from the center of the atom. (c) The converged ground-state electron density of the He atom was obtained from KS-DFT and rsDFT. (d) The total energy as a function of bond length of molecular H<sub>2</sub> from obtained from KS-DFT and rsDFT, respectively.

where the Chebyshev polynomial  $T_k(x)$  is the Chebyshev polynomial of the first kind.  $T_k(x)$  obeys the following recurrence relation:

$$T_{k+1}(x) + T_{k-1}(x) = 2xT_k(x)$$

with

$$T_0(x) = 1, T_1(x) = x.$$

In Table. S2, we present the number of nonzero Bessel function ( $N_{\text{Bessel}}$ ) as a function of time step  $\tau$ , and the corresponding number of total matrix-vector operations  $N_{\text{operations}}$  for the same propagation time  $T = 1024\pi$ . We can see a larger  $\tau$  leads to fewer operations with the same total propagation time.

#### 4. SINGLE ATOM

Let us consider a single Helium atom. In step (I), we construct a KS-Hamiltonian based on an initial electron density. In step (II), we obtain DOS  $D(\varepsilon)$  by using the time-evolution method without the diagonalization of the Hamiltonian matrix and subsequently determine the Fermi level  $\mu$  (see Fig. S4(a)).

As a comparison, the energies of KS orbitals from the diagonalization are also shown in Fig. S4(a), which agree very well with our results. In step (III), as there is only one occupied state, one can just use  $\rho_{\text{FD}}$  to obtain the electron

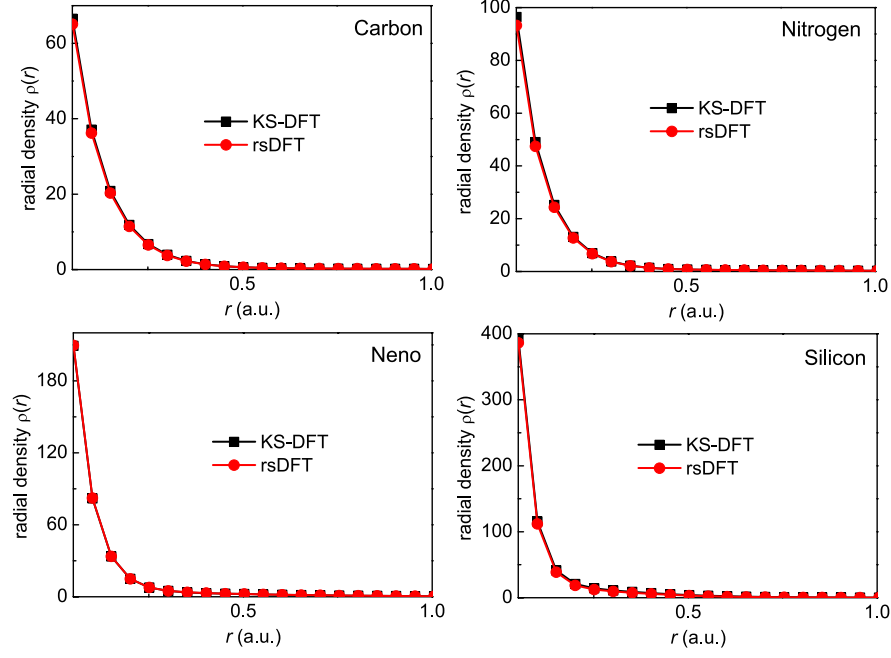


FIG. S5: Comparisons of ground-state charge density calculated by KS-DFT based on diagonalization and rsDFT of single atoms.

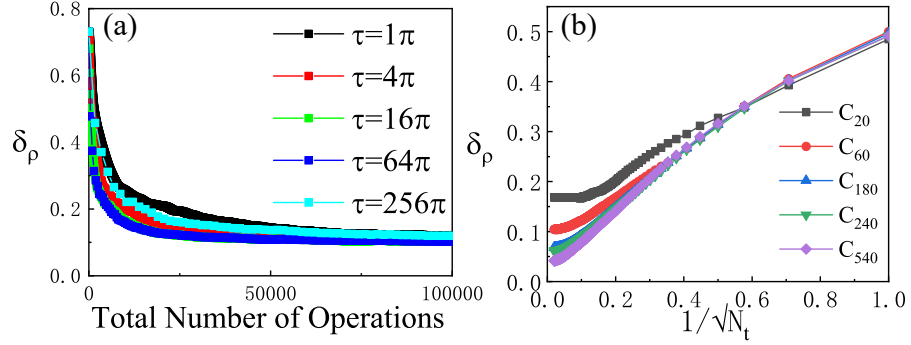


FIG. S6: (a) The statistical error  $\delta_\rho$  as a function of total operations. Different colour indicates different time step  $\tau$  in time evolution. (b) The statistical error  $\delta_\rho$  as a function of  $1/\sqrt{N_t}$  for different fullerenes, where  $\tau = 64\pi$ .

TABLE S2: The number of nonzero Bessel function ( $N_{Bessel}$ ) as a function of time step  $\tau$ , and the corresponding number of total matrix-vector operations  $N_{operations}$  for the same certain propagation time  $T = 1024\pi$ .

$\tau$	$N_{Bessel}$	$N_t$	$N_{operations}$
$\pi$	20	1024	20480
$2\pi$	27	512	13824
$4\pi$	38	256	9728
$8\pi$	56	128	7168
$16\pi$	89	64	5695
$32\pi$	149	32	4768
$64\pi$	261	16	4176
$128\pi$	478	8	3824
$256\pi$	899	4	3596
$512\pi$	1727	2	3454

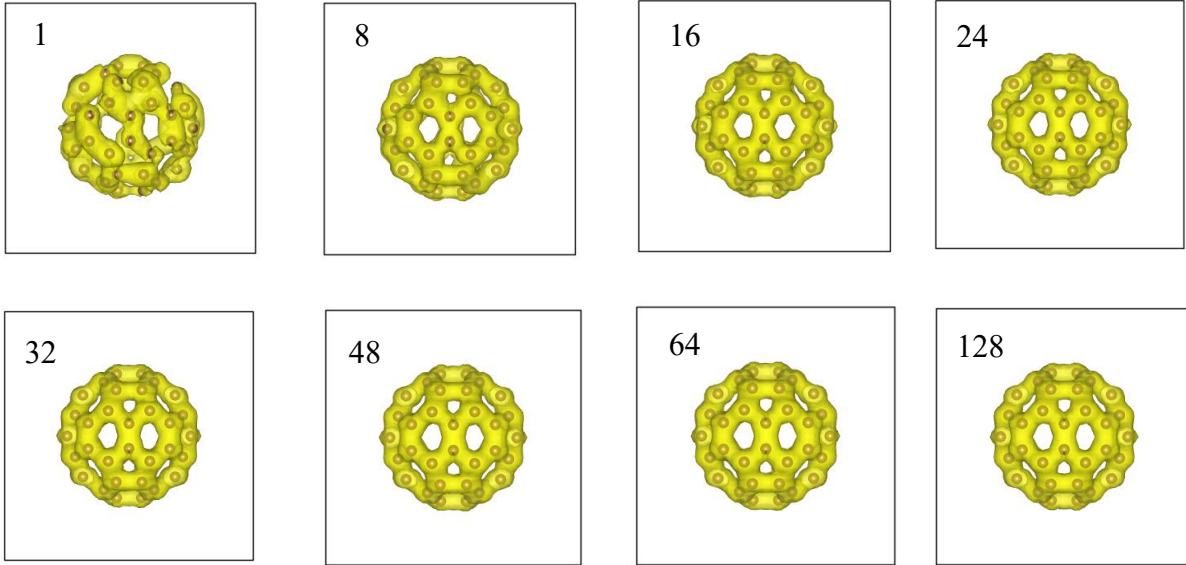
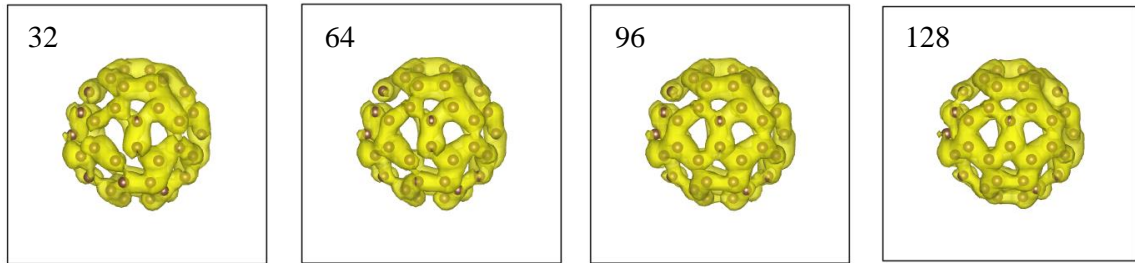


FIG. S7: The charge density of  $C_{60}$  calculated from average over a different number of random samples without time evolution.

(a) time intervals  $dt = \pi$



(b) time intervals  $dt = 32\pi$

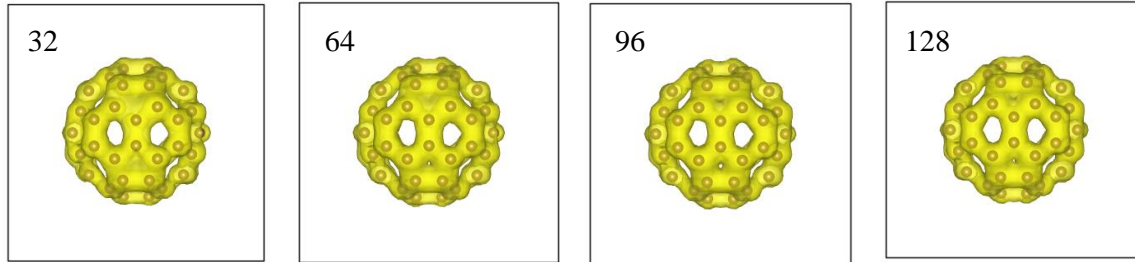


FIG. S8: The charge density of  $C_{60}$  calculated from one random state averaging over from time evolution for 32, 64, 96, 128 steps with  $dt=\pi$  (a) and  $dt=32\pi$  (b).

density without time evolution. As a comparison, we also calculate the electron density  $\rho_{diag}$  based on the occupied KS orbital obtained from the diagonalization of KS-Hamiltonian, and plot together with  $\rho_{FD}$  in Fig. S4(b). We see that with only  $S=10$  random samples,  $\rho_{FD}$  converges to  $\rho_{diag}$  with an error of  $\Delta(\rho_{FD} - \rho_{diag}) = 8.06 \times 10^{-5}$ , where  $\Delta(\rho_{FD} - \rho_{diag}) \equiv \sum_{j=1}^N |\rho_{FD}(\mathbf{r}_j) - \rho_{diag}(\mathbf{r}_j)|/N$ . In step (IV), we use  $\rho_{FD}$  as the new input electron density and perform the next iteration. The self-consistent iterations, including steps (I) to (IV), are continued until a threshold is reached. In our approach, since the space resolution (determined by  $N$ ) is much larger than the energy resolution (determined by  $N_t$ ), it is more accurate to use the electron density instead of the total energy to define the convergence

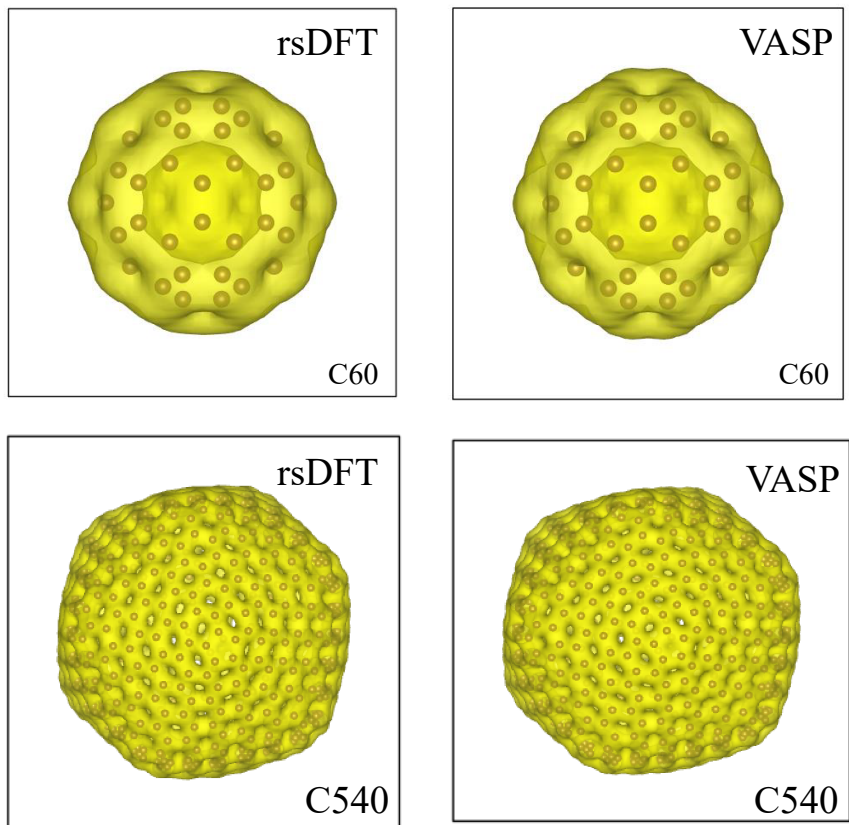


FIG. S9: The ground-state charge density calculated by rsDFT and VASP, respectively.

criterion. The ground-state electron density obtained from rsDFT without any diagonalization agrees well with the one from the common KS-DFT with diagonalization. Both are plotted in Fig. S4(c) for comparison. More examples of other single atoms can be found in Fig. S5.

#### 4. MOLECULES

For molecular systems, we consider a diatomic model  $H_2$ . The iterative calculations are similar to those of a single atom. Here we verify our approach by calculating the total energies for different H-H bond lengths and compare the results from our rsDFT approach and the common KS-DFT in Fig. S4(d). The two methods yield similar total energies for a given H-H bond length. The bond lengths in the ground state obtained from both ways are the same (74 pm), which agrees with the well-known result [7].

#### 5. CLUSTERS

We extend our calculations to large atomic clusters of fullerenes  $C_{60}$  and  $C_{540}$ . In Fig. S7, we plot the  $\rho_{FD}$  averaging from up to 128 random states. As a comparison, we also present  $\rho_{RS}$  using only one random state, but different propagation time in Fig. S8(a) with  $\tau = \pi$  and Fig. S8(b) with  $\tau = 32\pi$ . The real-space distribution of electron density in the ground state is visualized by VESTA [8] in Fig. S9. We use VASP (Vienna Ab initio Simulation Package) [9] to represent the standard KS-DFT method. VASP is a very efficient and widely used commercial KS-DFT package. The electron density distributions obtained from rsDFT and VASP are very similar.



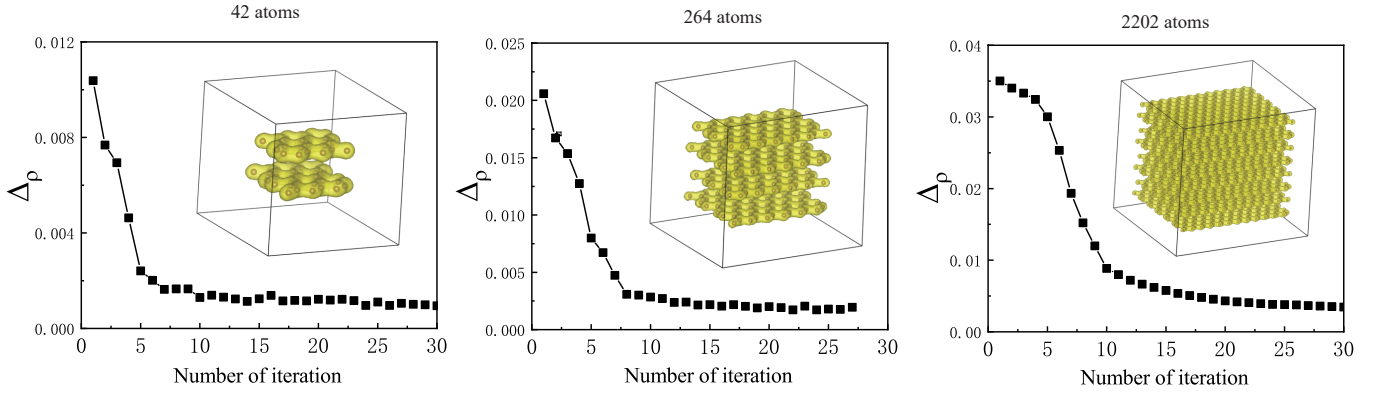


FIG. S10:  $\Delta(\rho_{in} - \rho_{out})$  as a function of iterative steps for A-B stacked graphite calculated by rsDFT. The insets indicate the converged ground state densities.

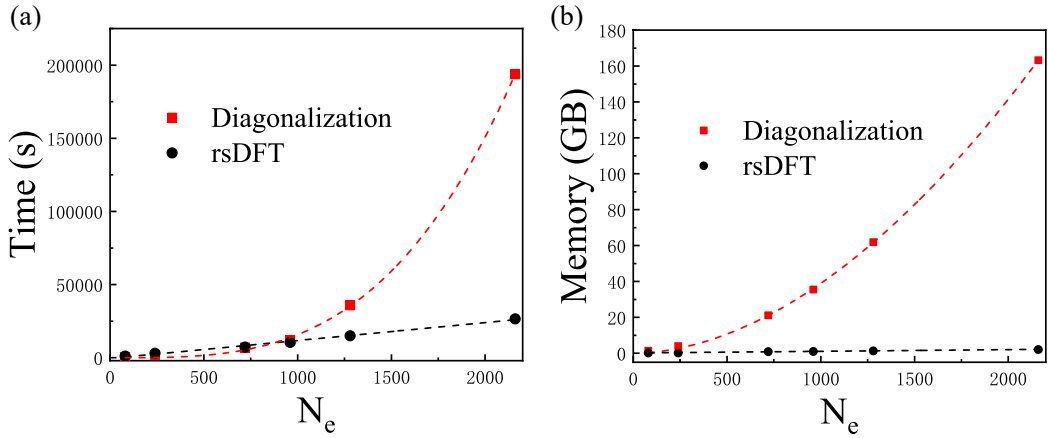


FIG. S11: Time cost of per iteration (a) and memory cost (b) during self-consistent calculations for fullerenes with different numbers of electrons. Black points refer to the traditional KS-DFT method with diagonalization, and red points refer to the rsDFT method without diagonalization. In rsDFT, we used 36 random samples for the average in the DOS and charge density calculations, the time step is  $\tau = 64\pi$  and the number of time steps is  $N_t = 36$ .

## 6. CRYSTALS

More rsDFT calculations of graphite nanocrystals with different numbers of carbon atoms are plotted in Fig. S10.

## 7. CPU TIME AND MEMORY COST

To have a direct comparison of the CPU time and memory cost between the traditional KS-DFT (with diagonalization) and rsDFT (without diagonalization), we performed calculations for the fullerenes with different numbers of atoms (electrons) on a server with 40 CPU cores (2\*Intel(R) Xeon(R) CPU Gold 6248). As shown in Fig. S11(a), if the system has less than  $\sim 1000$  electrons, the traditional KS-DFT is much faster, but when the system size reaches  $\sim 1000$  electrons, the rsDFT method becomes more efficient. The results in Fig. S11(a) also indicates that the time cost of rsDFT scales linearly with the system size, whereas the traditional KS-DFT scales approximately as  $O(N_e^3)$ . Although the accuracy of rsDFT and KS-DFT are not exactly the same, we estimate that rsDFT becomes more efficient when the system contains a few thousand or more electrons.

---

\* [s.yuan@whu.edu.cn](mailto:s.yuan@whu.edu.cn)

- [1] J. R. Chelikowsky, N. Troullier, and Y. Saad, *Phys. Rev. Lett.* **72**, 1240 (1994).
- [2] J. R. Chelikowsky, N. Troullier, K. Wu, and Y. Saad, *Higher-order finite-difference pseudopotential method: An application to diatomic molecules*, *Phys. Rev. B* **50**, 11355 (1994).
- [3] S. H. Vosko, L. Wilk, and M. Nusair, *Accurate spin-dependent electron liquid correlation energies for local spin density calculations: a critical analysis*, *Can. J. Phys.* **58**, 1200 (1980).
- [4] L. Kleinman and D. M. Bylander, *Efficacious Form for Model Pseudopotentials*, *Phys. Rev. Lett.* **48**, 1425 (1982).
- [5] ATOM, a program for DFT calculations in atoms and pseudopotential generation, distributed as part of the SIESTA software package. See <http://www.icmab.es/siesta/atom>.
- [6] D. R. Hamann, M. Schlüter, and C. Chiang, *Norm-Conserving Pseudopotentials*, *Phys. Rev. Lett.* **43**, 1494 (1979).
- [7] K.-P. Huber, *Molecular spectra and molecular structure: IV. Constants of diatomic molecules* (Springer Science & Business Media, 2013).
- [8] K. Momma and F. Izumi, *VESTA: a three-dimensional visualization system for electronic and structural analysis*, *J. Appl. Crystallogr.* **41**, 653 (2008).
- [9] G. Kresse and J. Furthmüller, *Efficiency of ab-initio total energy calculations for metals and semiconductors using a plane-wave basis set*, *Comput. Mater. Sci.* **6**, 15 (1996).